International Journal of Research in Engineering and Science (IJRES)
ISSN (Online): 2320-9364, ISSN (Print): 2320-9356
www.ijres.org Volume 14 Issue 3 ǁ March 2026 ǁ PP. 205-222

Design of novel DAPY derivatives as HIV-1 RT inhibitors based on 3D-QSAR, molecular docking, and molecular dynamics simulations

Xi He,[a] Yankai Li, [a] and Shuping Zhang,[a]*
[a]*Department of Chemistry, University of Shanghai for Science and Technology, Shanghai 200093, P. R. China*

Abstract
HIV-1 reverse transcriptase (RT) is a key target for antiretroviral therapy. However, resistance to non-nucleoside reverse transcriptase inhibitors (NNRTIs) remains a long-standing problem. This study integrates three-dimensional quantitative structure-activity relationship (3D-QSAR), molecular docking, molecular dynamics (MD) simulations, and ADMET profiling techniques to elucidate the structure-activity- relationship (SAR) of diarylpyrimidine (DAPY) derivatives and guide inhibitor design. 3D-QSAR models were established using CoMFA and CoMSIA-SED, showing good performance (CoMFA: $q^2 = 0.602$, $r^2 = 0.969$, $F = 103.311$; CoMSIA-SED: $q^2 = 0.629$, $r^2 = 0.992$, $F = 273.483$). Contour maps highlighted key steric, electrostatic, and hydrogen-bond donor features associated with potency. Furthermore, molecular docking also explored the mechanism of interaction between small molecules and receptor proteins. Based on the insights from the model and docking, eight new DAPY derivatives were designed using the most active template compound (Compound 11), and their predicted activities were all superior to the template compound. Subsequent MD simulations supported the formation of stable complexes. ADMET profiling suggested acceptable drug-like properties. Overall, this study provides computationally derived SAR guidance and prioritized candidates for further optimization and experimental validation.
Keywords: *DAPY derivative; QSAR; molecular docking; MD simulation; ADMET*

Date of Submission: 15-03-2026 Date of Acceptance: 31-03-2026

I. Introduction

Human immunodeficiency virus type 1 (HIV-1) infection remains a major global health challenge despite the widespread use of combination antiretroviral therapy. [1-5] HIV-1 reverse transcriptase (RT), an essential enzyme responsible for viral genome replication, has long been recognized as a primary target for antiretroviral drug development. [6-8]Among RT inhibitors, non-nucleoside reverse transcriptase inhibitors (NNRTIs) play a critical role in highly active antiretroviral therapy due to their high potency and favorable selectivity. [9-12]However, the rapid emergence of drug-resistant viral strains driven by RT mutations continues to compromise the long-term clinical efficacy of currently approved NNRTIs, underscoring the need to develop novel inhibitors with improved resistance profiles.[13]

RT catalyzes the reverse transcription of the viral single-stranded RNA genome into double-stranded DNA, which subsequently integrates into the host genome to enable persistent infection and viral propagation. Direct inhibition of RT thus effectively blocks this essential replication step, suppressing viral proliferation at its source.[7, 8, 13] Against this backdrop, diarylpyrimidine (DAPY) derivatives have attracted sustained interest as next-generation NNRTI scaffolds owing to their favorable structural characteristics and potent bioactivity.[14] Structurally, these compounds possess a pyrimidine core flanked by aryl substituents, a feature that facilitates stable engagement with the non-nucleoside binding site (NNBS) of HIV-1 RT. Importantly, DAPY derivatives exhibit pronounced structural plasticity: systematic modification of the aryl moieties allows flexible tuning of molecular conformation, electronic distribution, and hydrophobicity, thereby mitigating the adverse impact of resistance-associated mutations on ligand binding.[15] Consistent with this property, multiple DAPY analogues retain inhibitory potency against HIV-1 variants carrying common resistance mutations, underscoring their value as privileged scaffolds for overcoming NNRTI resistance.[16-19] Nevertheless, the key structural determinants governing the structure activity relationship (SAR) of DAPY derivatives, particularly the interplay between aryl substitutions and anti-resistance capacity—remain incompletely elucidated, which limits the rational optimization of these molecules.

To address this knowledge gap, further elucidate the SAR of DAPY derivatives, and guide the rational optimization of superior anti-HIV-1 candidates, we conducted an integrated computational investigation on 34 reported DAPY compounds with available anti-HIV-1 activity data. Our workflow integrated three-dimensional

quantitative structure-activity relationship (3D-QSAR) modeling, molecular docking, molecular dynamics (MD) simulations, and in silico ADME/T evaluation. Specifically, 3D-QSAR analysis quantified the contribution of three-dimensional molecular features to bioactivity, identifying steric, electrostatic, and hydrophobic determinants that provide explicit guidelines for structural optimization.[20] Molecular docking was then employed to characterize plausible binding orientations within the RT NNBS, rationalizing activity differences from a structure-based interaction perspective.[21] To account for protein-ligand flexibility and solvent effects under near-physiological conditions, MD simulations were performed to examine binding dynamics and complex stability, which further validated our proposed design rationale.[22] By integrating these complementary computational approaches, we designed eight novel DAPY derivatives with favorable predicted efficacy, providing computationally guided candidates and mechanistic insights to support subsequent inhibitor development.

II. Materials And Methods

2.1 Database screening and biological activity

In this study, we collected chemical structures and activity information for 34 DAPY compounds and their derivatives from published literature.[1] To construct and evaluate the predictive models, the entire dataset was randomly divided into two subsets: one serving as the training set (comprising 27 compounds) for model development, and the other as the test set (including the remaining 7 compounds) for assessing the model's reliability and predictive performance. During dataset construction, particular attention was paid to preserving both the structural diversity of the compounds and a representative distribution of activity values, thereby supporting the generalizability of the resulting models. Experimental activities were reported as EC50 (half-maximal effective concentration) values and were uniformly transformed into pEC50 values (pEC50 = -log EC50),[23] which were used as the dependent variable in subsequent 3D-QSAR analyses. The chemical structures and pEC50 values of all compounds are summarized in Table 1, with test-set molecules indicated by an asterisk ("*"). Furthermore, Table 1 provides the residuals between experimentally measured and model-predicted pEC50 values for each compound. The selected dataset covers a consistent activity window (pEC50 = 7.119-8.858), which is suitable for establishing and validating quantitative structure-activity relationship models.

Table 1. The structure and activity of the 34 molecules in the dataset.

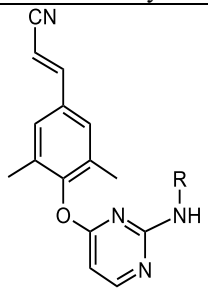

NO	R	EC_{50}(μM)	pEC50	Predicted activity (pEC50) CoMFA	Residual	CoMSIA	Residual
01	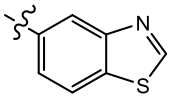	0.0019	8.721	8.754	-0.032	8.722	-0.0007
02*	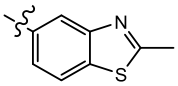	0.0120	7.920	7.978	-0.057	8.098	-0.177
03	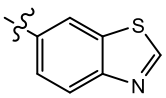	0.0089	8.050	8.032	0.018	8.057	-0.006
04*	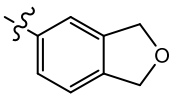	0.0019	8.721	8.681	0.040	8.123	0.598
05	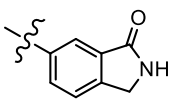	0.0064	8.193	8.198	-0.004	8.182	0.011

06	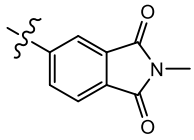	0.0056	8.251	8.244	0.007	8.222	0.029
07	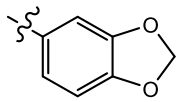	0.0078	8.107	7.935	0.172	8.030	0.077
08	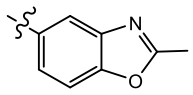	0.0077	8.113	8.124	-0.010	8.163	-0.049
09	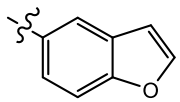	0.0069	8.161	8.169	-0.007	8.179	-0.017
10	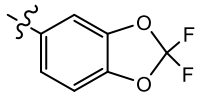	0.0200	7.698	7.955	-0.256	7.816	-0.117
11	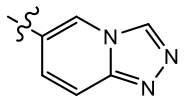	0.0019	8.721	8.777	-0.055	8.728	-0.006
12*	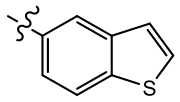	0.0077	8.113	8.204	-0.090	8.641	-0.527
13	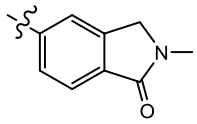	0.0310	7.508	7.508	0.0006	7.535	-0.026
14	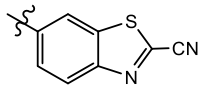	0.0610	7.214	7.178	0.036	7.164	0.050
15	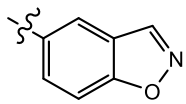	0.0067	8.173	8.187	-0.013	8.241	-0.067
16	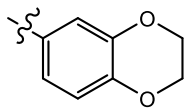	0.0140	7.853	7.917	-0.063	7.871	-0.017
17	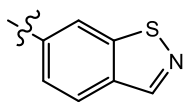	0.0024	8.619	8.422	0.197	8.549	0.070
18*	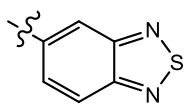	0.0072	8.142	8.018	0.124	7.618	0.524
19	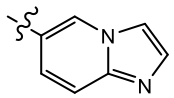	0.0020	8.698	8.663	0.035	8.692	0.006
20	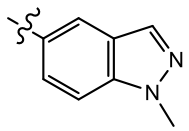	0.0028	8.552	8.548	0.004	8.527	0.025
21	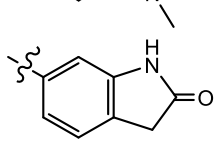	0.0018	8.744	8.747	-0.002	8.734	0.010
22	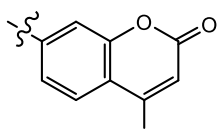	0.0180	7.744	7.701	0.043	7.752	-0.007

23	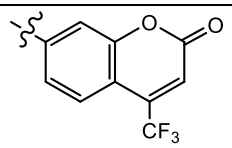	0.0760	7.119	7.134	-0.014	7.071	0.048
24	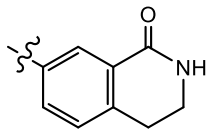	0.0026	8.858	8.606	-0.020	8.587	-0.001
25	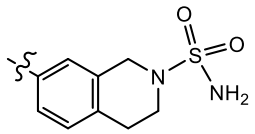	0.0160	7.795	7.872	-0.076	7.807	-0.011
26*	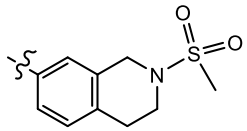	0.0063	8.200	7.963	0.237	7.631	0.569
27	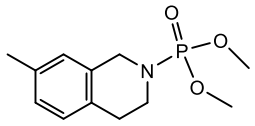	0.0120	7.920	7.905	0.015	7.928	-0.007
28	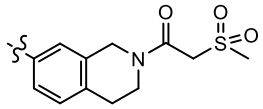	0.017	7.769	7.739	0.030	7.785	-0.015
29*	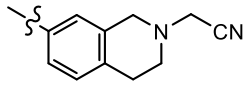	0.0370	7.431	7.595	-0.163	8.173	-0.741
30	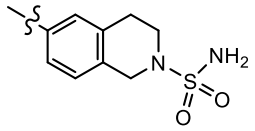	0.0083	8.080	8.083	-0.002	8.066	0.014
31	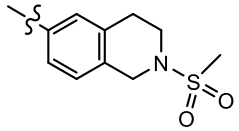	0.0068	8.167	8.165	0.002	8.166	0.001
32	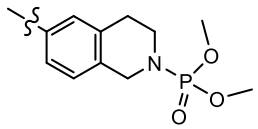	0.0081	8.091	8.092	-0.001	8.095	-0.003
33	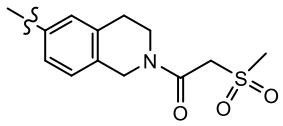	0.0093	8.031	8.037	-0.005	8.027	0.004
34*	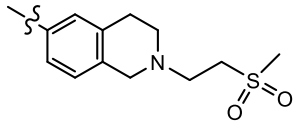	0.0190	7.721	7.928	-0.206	8.167	-0.445

2.2 Optimization and alignment of compound structures

The first step in the molecular modeling workflow was to generate 2D sketches for all compounds in the dataset. The 3D structures of the 34 DAPY derivatives were built using the sketch module in SYBYL-X 2.0 (Windows 10). Gasteiger-Hückel partial charges were assigned, and the structures were energy-minimized using the Tripos force field. Geometry optimization was performed with the Powell conjugate-gradient method, using a maximum of 1000 iterations and a convergence criterion of 0.005 kcal·mol^{-1}, while other parameters were kept at the default settings.[24-26] The minimized conformations were subsequently used for molecular alignment prior to CoMFA and CoMSIA modeling. Because molecular alignment critically influences the quality and predictivity of

3D-QSAR models, a common-substructure alignment strategy was adopted in this study. The shared scaffold used for alignment is highlighted in blue in Figure 1a. Among all compounds, Compound 11 showed the highest inhibitory activity (EC50 = 0.0019 μM) and contains the representative common core; therefore, it was selected as the alignment template. The resulting superposition of the dataset aligned to this common substructure is shown in Figure 1b, indicating a consistent overlap of the shared core across the series. This alignment protocol has been widely used for scaffold-consistent series and provides interpretable contour map features.

Figure 1

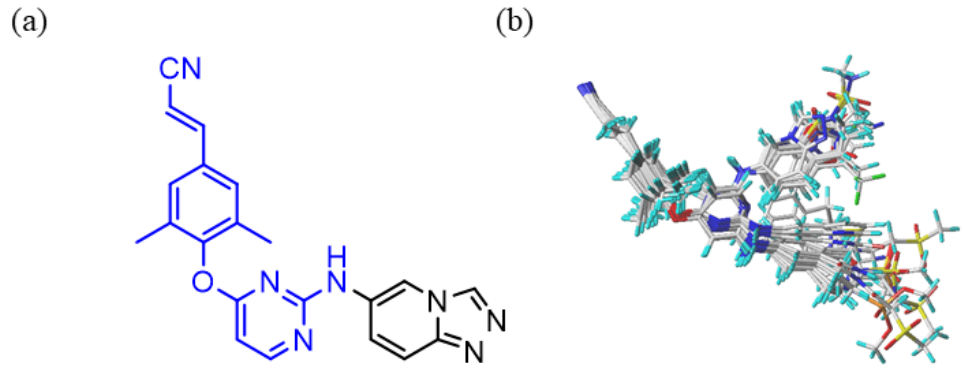

Figure_1. (a) Chemical structure of Compound 11; the shared scaffold used for molecular alignment is highlighted in bold blue. (b) Superposition of all compounds aligned to the template (Compound 11).

2.3 Development of 3D-QSAR models

3D-QSAR modeling is widely used to relate biological activity to the spatial distribution of physicochemical fields around aligned ligands. Among 3D-QSAR approaches, Comparative Molecular Field Analysis (CoMFA) and Comparative Molecular Similarity Indices Analysis (CoMSIA) are the most frequently applied methods for extracting interpretable SAR features.[27] In CoMFA, steric (van der Waals/Lennard-Jones) and electrostatic field values are sampled on a 3D lattice surrounding a set of consistently aligned molecules, typically using a probe atom, and partial least squares (PLS) analysis is then employed to correlate the field descriptors with experimental activity values to generate predictive models.[28] CoMSIA follows a similar modeling framework but extends the field descriptors by incorporating additional similarity indices, such as hydrophobic, hydrogen-bond donor, and hydrogen-bond acceptor fields. A key advantage of CoMSIA is the use of a Gaussian-type distance dependence, which produces smoother field contributions and avoids the strong distance-dependent singularities commonly associated with CoMFA potentials, thereby facilitating more stable contour map interpretation.[29]

2.4 Model verification

3D-QSAR models were constructed via partial least squares (PLS) regression,[30] correlating structural features with experimental pEC50 values. Cross-validation was performed using the Leave-One-Out (LOO) method to the optimal number of components (ONC) and the cross-validation correlation coefficient are obtained. (q^2). Subsequently, non-cross-validation methods were employed to obtain additional evaluation parameters associated with the CoMFA and CoMSIA models, such as the correlation coefficient (r^2), significance test value (F), and standard error of estimate (SEE). A reliable model should meet the following criteria: $q^2 > 0.5$, $r^2 > 0.9$, $F > 100$, and SEE significantly less than 1.[31] The formulas used to calculate q^2 and r^2 are presented in formula (1) and (2), respectively, where Y_{pred}, $\bar{Y}_{pred}$, Y_{exp}, and $\bar{Y}_{exp}$ denote the predicted activity values, mean predicted activity, experimental activity values, and mean experimental activity of compounds in the training set.[32]

$$q^2 = 1 - \frac{\sum(Y_{pred} - Y_{exp})^2}{\sum(Y_{exp} - \bar{Y}_{pred})^2} \quad \ldots\ldots (1)$$

$$r^2 = \frac{[\sum(Y_{exp} - \bar{Y}_{exp})(Y_{pred} - \bar{Y}_{pred})]^2}{\sum(Y_{pred} - \bar{Y}_{pred})^2 \times \sum(Y_{pred} - \bar{Y}_{pred})^2} \quad \ldots\ldots (2)$$

Relying solely on favorable internal validation results is insufficient to confirm the credibility of 3D-QSAR model. To further evaluate the model's actual predictive capability and reliability, external validation is additionally required. The formula for calculating the external validation coefficient (r_{pred}^2) is presented in formula (3), which serves as the primary parameter for assessing the external predictive performance of the model. An

r^2_{pred} value greater than 0.6 indicates that the model possesses good external predictive capability. In formula (3), SD denotes the sum of squared deviations between the mean activity value of compounds in the training set and the activity value of each compound in the test set, while PRESS denotes the sum of squared deviations between the experimental activity values and predicted activity values of compounds in the test set.[33]

$$r_{pred}^2 = 1 - \frac{PRESS}{SD} \quad \text{..... (3)}$$

In addition to r_{pred}^2, several complementary external validation metrics were calculated to provide a more stringent assessment of model reliability, including r^2, k, k', r_0^2, $r_0'^2$, r_m^2, $r_m'^2$and Δr_m^2, A 3D-QSAR model was regarded as acceptable when it satisfied the commonly used thresholds: $r^2 > 0.6$, $0.85 < k$ (or k') < 1.15, r_m^2 (or $r_m'^2$) > 0.5, $(r^2 - r_0^2)/r^2 < 0.1$, and $\Delta r_m^2 < 0.2$.[34]

2.5 Design and activity prediction of novel inhibitors

The present study aimed to design novel DAPY derivatives with enhanced activity as HIV-1 RT inhibitors. Based on the contour plots generated by the validated CoMFA and CoMSIA-SED models, we analyzed the key structural features governing biological activity, and identified the critical modification sites of the highly active template molecule (Compound 11) as well as the required substituent properties.[35] Subsequently, using the energy-minimized Compound 11 as the template for the design and alignment of new molecules, we predicted the activity of these molecules using the trained CoMFA and CoMSIA-SED models, and screened for novel compounds with enhanced activity. Finally, comprehensive activity validation of these new compounds was performed via molecular docking, ADMET prediction, MD simulations, and binding free energy calculations.

2.6 Molecular docking

Molecular docking is a key method for validating the binding patterns of small molecules with proteins and elucidating the pharmacological mechanisms of drug molecules, thereby promoting novel drug innovation and discovery to provide new therapeutic options for specific diseases.[36] This study employed the Surflex-Dock module within SYBYL X-2.0 software for molecular docking. The 3D crystal structure of the target protein (HIV-1 RT) was obtained from the RCSB Protein Data Bank (PDB ID: 8FE8. https://www.rcsb.org/). The target protein underwent a series of preprocessing steps, including water molecule removal, amino acid residue repair, hydrogen atom addition, and charge assignment. Following protein optimization, newly designed compounds were processed using identical parameter settings and workflows. In docking mode, we computed initial 3D conformations for the new compounds, optimized their structures, and successfully generated docking pockets where these compounds interacted with the pre-defined protein binding site. Based on this, optimal molecular conformations were selected, and the molecular docking results were visualized using PyMOL software.[37] As a bridge connecting "target protein mechanism research" and "novel drug molecule design", molecular docking makes the elucidation of pharmacological mechanisms more concrete, accelerating the transformation from basic scientific discoveries to clinical therapeutic drugs.[38]

2.7 MD simulations

MD simulations were conducted to assess the conformational stability of the docked HIV-1 RT-ligand complexes under explicit-solvent conditions. All simulations were performed with GROMACS 2019.[39] First, the protein structure was retrieved from the RCSB Protein Data Bank (PDB ID: 8FE8), and crystallographic water molecules and non-relevant ligands were removed in PyMOL 2.0 prior to system setup. The protein was described using the AMBER99SB-ILDN force field, whereas ligand parameters were generated with the General Amber Force Field (GAFF). Ligand topology files and atomic charges were prepared using Amber 20 based on quantum-chemical calculations and RESP charge fitting. The protein and ligand topologies were then combined to build the full complex topology. Each complex was embedded in a dodecahedral periodic box with a minimum solute–box distance of 1.0 nm and solvated using the SPC/E water model. Counterions (Na^+ and Cl^-) were added to neutralize the system. Energy minimization was performed using the steepest descent algorithm for up to 50,000 steps to remove unfavorable contacts. The systems were subsequently equilibrated under NVT and NPT ensembles (100 ps each) at 300 K and 1 atm. Production MD simulations were then carried out for 100 ns with a 2 fs integration step. The LINCS algorithm was applied to constrain bonds involving hydrogen atoms. Finally, trajectory analyses included the root-mean-square deviation (RMSD), root-mean-square fluctuation (RMSF), and radius of gyration (Rg) to characterize overall stability and structural flexibility of the complexes. For binding

free-energy estimation, the equilibrated portion of each trajectory was extracted from the last 20 ns and analyzed using the gmx_MMPBSA tool. In addition, free energy landscape (FEL) analysis was performed to identify dominant conformational basins of the complexes and to further evaluate their stability trends.[40, 41]

2.8 ADMET

In the drug research and development process, absorption, distribution, metabolism, excretion, and toxicity (ADMET) serve as the core pharmacokinetic and toxicological properties of drugs, and the unpredictability of these properties often constitutes a critical bottleneck. This not only significantly hinders research and development efficiency, but also easily leads to substantial resource redundancy and waste. However, traditional ADMET evaluation methods relying on *in vitro* biological experiments suffer from the drawbacks of high cost and long turnaround time, and are also unable to meet the demand for rapid screening of large-scale compounds.[42] With the rapid advancement of pharmacoinformatics, this long-standing challenge in the field has been significantly addressed, and a variety of efficient ADMET property prediction methods have been developed. In this study, two specialized online tools, ADMETlab2.0[43] and pkCSM,[44] were employed to systematically evaluate the pharmacokinetic and toxicological properties of the newly designed compounds, thereby establishing a critical data foundation and decision-making basis for subsequent drug research and development efforts.

III. Results and discussion

3.1 Analysis and statistical validation of 3D-QSAR models

In this study, we evaluated the reliability of the CoMFA and CoMSIA models by comparing the residuals between the predicted values and actual values of the models, as shown in Figure 2. The results showed that all actual residual values did not exceed 0.5, indicating that both models possess good reliability. To further verify the predictive accuracy and stability of the constructed CoMFA and CoMSIA models, we conducted rigorous internal and external validation. The results are presented in Tables 2 and 3. For the CoMFA model, the ONC was determined to be 6 using the Leave-One-Out method, yielding a q^2 of 0.602 (greater than 0.5). Based on this, PLS analysis was performed, and the calculated r^2, SEE, and F were 0.969, 0.088, and 103.311, respectively. The contribution rates of the electrostatic field (E) and steric field (S) to the model were 0.445 and 0.555, respectively. This indicates that the CoMFA model not only meets the requirements for internal validation but also exhibits significant predictive reliability and stability.

In contrast, the CoMSIA model further incorporates hydrogen bond donor, hydrogen bond acceptor, and hydrophobic fields on the basis of the original steric and electrostatic fields, thereby markedly enhancing the stability and reliability of the model. We constructed a series of CoMSIA models with different field combinations and ultimately selected the CoMSIA-SED model with the highest q^2 and r^2 values for subsequent analysis. In this model, the contribution rates of the steric field (S), electrostatic field (E), and hydrogen bond donor field (D) were calculated as 18.3%, 53.8%, and 27.9%, respectively. This indicates that the electrostatic field and hydrogen bond donor field are key factors governing the biological activity of the compounds, providing important basis for the subsequent molecular optimization and design. Figure 3 presents the scatter plots of the observed activity values from the dataset against the predicted values of the CoMFA and CoMSIA-SED models. The data show that the scatter plots exhibit a strong linear trend, with both the test set and training set distributed on both sides of the regression line. This confirms the reliability of the models and their application value in predicting the activity of novel molecules.

To further verify the stability and accuracy of the models, external validation was additionally performed. As shown in Table 3, both the CoMFA and CoMSIA-SED models exhibited good predictive performance, with the external validation correlation coefficient (r_{pred}^2) reaching 0.848, which exceeds the threshold of 0.6. In addition, the k values of both models ranged from 0.85 to 1.15, and their r^2 values were 0.567 and 0.535, respectively, both surpassing the threshold of 0.5. Other parameters also met the required criteria, further confirming the high reliability of the models. After comprehensively analyzing all statistical parameters, the constructed CoMFA and CoMSIA-SED models demonstrate excellent robustness and predictive capability, and can be reliably used for subsequent SAR analysis and compound activity prediction.

Figure 2

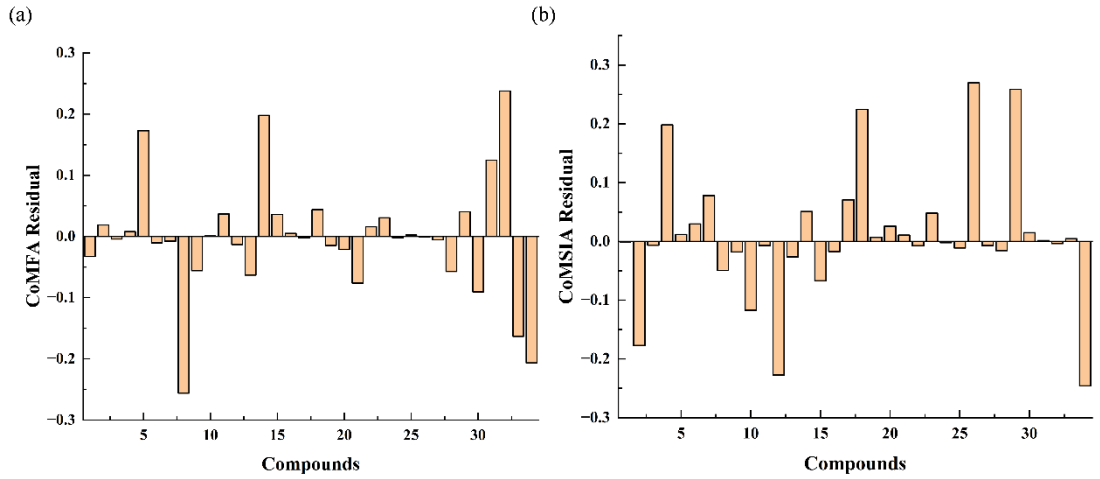

Figure_2. Residual plots for (a) CoMFA and (b) CoMSIA

Table 2. The optimal statistical results of the CoMFA and CoMSIA models

	LOO	Non-cross-validation			Field contribution (%)				
Model	ONC	q^2	r^2	SEE	F	D	S	E	H	A
CoMFA	6	0.602	0.969	0.088	103.311	——	55.5	44.5	——	——
CoMSIA-SED	8	0.629	0.992	0.048	273.483	27.9	18.3	53.8	——	——

Figure 3

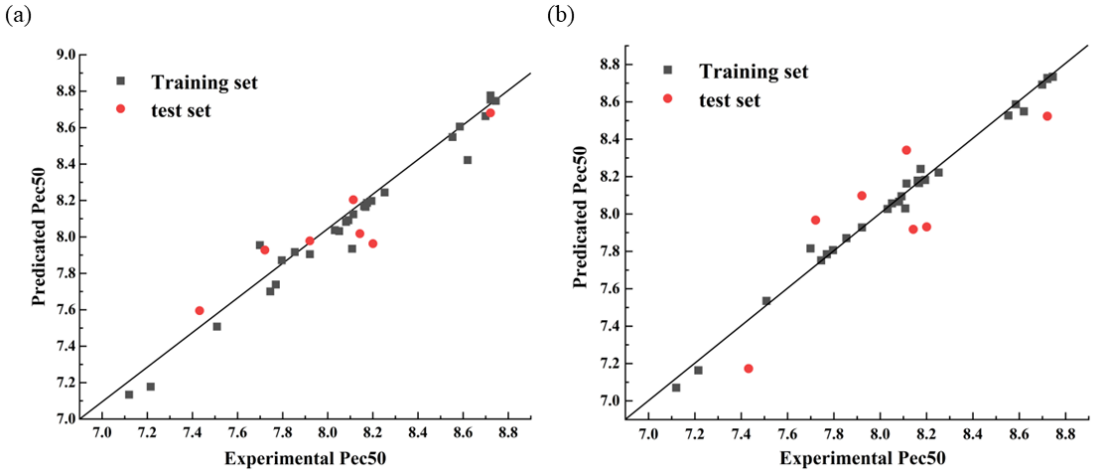

Figure_3. Scatter plots comparing experimental and predicted pEC50 values (a) CoMFA and (b) CoMSIA-SED models.

Table 3. External Validation Results of 3D-QSAR Studies

Parameter	Validation criteria	CoMFA	CoMSIA-SED
r_{pred}^2	r_{pred}^2>0.6	0.848	0.848
k	0.85≤k≤1.15	0.998	0.998
K'	0.85≤K′≤1.15	1.001	1.001
r_0^2	/	0.978	0.897
$r_0'^2$	/	0.875	0.955
r_m^2	r_m^2>0.5	0.567	0.535
$r_m'^2$	r_m^2>0.5	0.587	0.542
Δr_m^2	$\Delta r_m'^2$<0.2	0.0002	0.003
r^2_m	r^2_m>0.5	0.577	0.534
$(r^2-r_0^2)/r^2$	$(r^2-r_0^2)/r^2$<0.1	-0.139	-0.045
$(r^2-r_0'^2)/r^2$	$(r^2-r_0'^2)/r^2$<0.1	-0.019	-0.113

3.2 3D-QSAR contour map analysis

The contours map of the CoMFA model are presented in Figure 4, with Compound 11 selected as the template molecule. Figure 4a shows the contour map of the steric field. In guiding the design of new molecules, the green regions indicate that incorporating bulkier substituents exerts a beneficial effect on the compounds, while the yellow regions suggest that using smaller substituents is favorable for enhancing molecular activity. From the figure, the large green contour surrounding the R1 substituent indicates that introducing bulkier groups here can enhance the inhibitory activity of the compound. This explains why the activity is higher when the R1 position is substituted with a dichlorophenyl group (A03/pEC50 = 10.391) than when the R1 position is substituted with a difluorophenyl group (A01/pEC50 = 9.234). Figure 4b presents the contour map of the electrostatic field in the CoMFA model. The red regions indicate that the introduction of high electronegativity groups is favorable for enhancing activity, while the blue regions show that the addition of positive charges contributes to boosting activity. As observed in Figure 4b, there are one large and one small red region around R1, suggesting that introducing electronegative groups here is beneficial for boosting inhibitory activity. For example, the incorporation of difluorophenyl, dichlorophenyl, and pyridyl groups all resulted in increased activity, with the new compounds exhibiting varying levels of potency. The activity of newly designed compounds predicted by the CoMFA model all exceeds that of the template compound (Compound 11, CoMFA-predicted activity = 8.777), ranging from 8.957 to 10.391. This further validates the stability and reliability of the model.

Figure 4

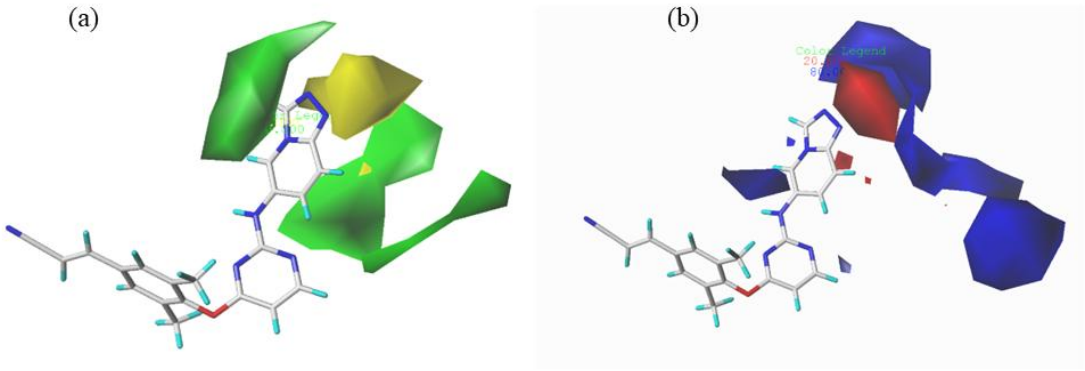

Figure_4. The CoMFA contour of template molecule 11. (a) Steric field. (b) Electrostatic field.

Figure 5 presents the contour maps of the steric field, electrostatic field, and hydrogen bond donor field of the CoMSIA-SED model. The contours of the steric field and electrostatic field of the CoMSIA-SED model are similar to those of the CoMFA model, as shown in Figure 5a and 5b, where the meanings of the various color blocks are consistent with those in the CoMFA model. From the hydrogen bond donor field (Figure 5c), it can be seen that blue block regions are favorable for the introduction of hydrogen bond donor groups, while purple regions show the opposite. This indicates that adding groups capable of donating hydrogen bonds at these positions can enhance the activity of the compounds. For instance, the introduction of amino groups and sulfonylamino groups as hydrogen bond donors both contributes to increased activity. Notably, for the new molecule A05 (pEC50 = 10.369), the introduction of a large-volume aromatic ring at the R1 position meets the requirements of the green region in the steric field and the red region in the electrostatic field simultaneously, and the R2 position is substituted with a hydrogen bond donor group. However, its activity is slightly lower than that of A03 (pEC_{50} = 11.472), which is because the electronegativity of the tert-butyl group is lower than that of dichlorobenzene. This is also consistent with the rule that the electrostatic field dominates activity. For compound A04 (pEC_{50} = 9.387), the reason for its lowest activity may be that the sulfonylamino group at the R2 position, although acting as a hydrogen bond donor, does not fit the steric field, which offsets part of the activity gain. This also confirms the necessity of the synergy among the three fields. By providing a more detailed understanding of the SAR of the compounds, these CoMSIA-SED models can guide the structural modification and optimization of compounds. The CoMSIA-SED results further validate the conclusions drawn, with predicted activities ranging from 9.383 to 11.472, which are higher than that of Compound 11 (CoMSIA-predicted activity = 8.728).

Figure 5

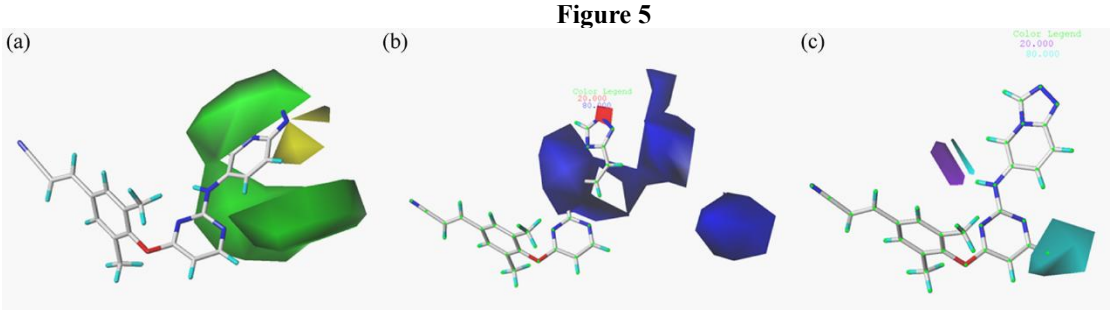

Figure_5. The CoMSIA contour of template molecule 11. (a) Steric field. (b) Electrostatic field. (c) Hydrogen bond donor field.

3.3 Design and activity prediction of new molecules

To advance the development of HIV-1 drugs, the established 3D-QSAR models (CoMFA and CoMSIA-SED) and their contour plots can serve as important reference standards, which hold significant benefits for enhancing drug innovation capabilities and therapeutic efficacy. Lead compound 11 is suitable as a template molecule for structural modification. Specifically, its activity can be enhanced by incorporating larger substituents, electronegative groups, and hydrogen bond donor groups. Based on this, we designed eight novel DAPY derivative anti-HIV inhibitors, and their pEC50 values were predicted using the constructed 3D-QSAR models. The newly designed molecular structures and their corresponding predicted values are shown in Table 4. Notably, the predicted activity of all eight newly designed molecules exceeds that of Compound 11, fully demonstrating their potential as anti-HIV inhibitors. However, further validation through *in vitro* or *in vivo* experiments remains necessary to confirm the actual efficacy of these new molecules.

Table 4. Involved information of the template compound and the newly designed compounds

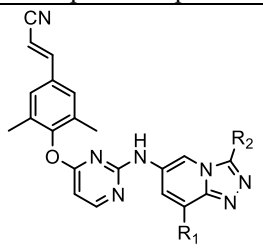

NO.	R1	R2	Predicted activity	
			CoMFA	CoMSIA
A01	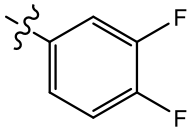		9.234	10.320
A02	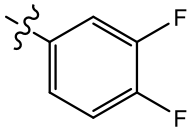	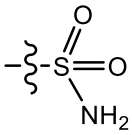	9.601	10.203
A03	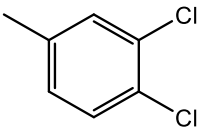		10.391	11.472
A04	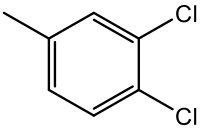	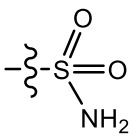	8.957	9.387
A05	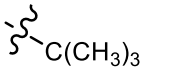		10.323	10.369

A06	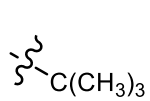	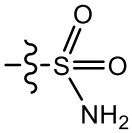	9.374	10.456
A07	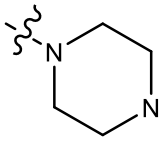		9.213	9.463
A08	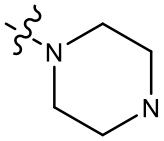	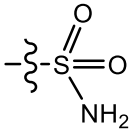	9.877	9.4788

3.4 Molecular docking simulations results

Molecular docking is widely used in structure-based drug discovery to characterize ligand–receptor binding modes and to support lead optimization. In this study, the co-crystallized ligand was extracted from HIV-1 RT (PDB: 8FE8), and the NNRTI binding pocket is shown in Figure 6a.[45] The docking protocol was validated by redocking the native ligand into the same pocket using Surflex-Dock. The redocked pose reproduced the crystallographic binding mode with a high degree of overlap (Figure 6b), supporting the reliability of the adopted docking settings. Subsequently, Compound 11, identified as the most active molecule in the dataset, together with the eight newly designed derivatives, was docked into 8FE8 using the same protocol and parameter settings. Based on the activity rankings predicted by both 3D-QSAR models (CoMFA: 8.777; CoMSIA: 8.728), Compounds A04 and A03 were selected for further analysis as the lowest- and highest-ranked candidates, respectively.

Figure 6

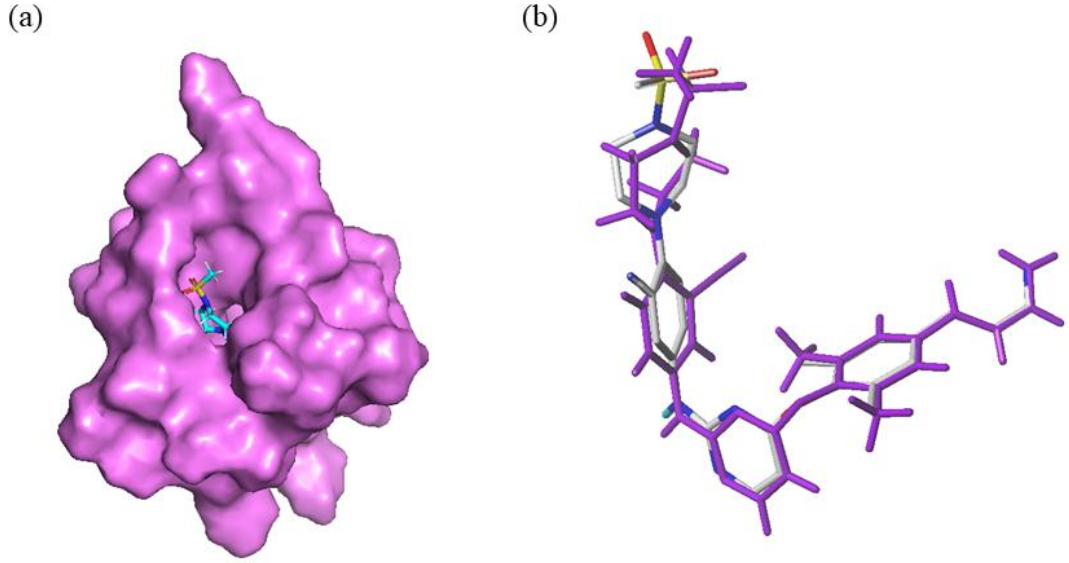

Figure_6. Re-docking verification results of co-crystallized ligand. (a) View of the binding pocket. (b) Comparison of the initial and re-docked poses (white, pre-docking; purple, re-docked).

The docking results of Compound 11, as shown in Figure 7, demonstrate favorable matching within the active site. Compound 11 forms multiple hydrogen bonds with key residues: an oxygen atom acts as a hydrogen-bond acceptor to LYS101 (2.71 Å), and the pyrimidine-ring nitrogens form hydrogen bonds with LYS101 (2.40 Å) and LYS103 (2.90 Å), respectively. In addition, the phenoxy moiety forms hydrophobic contacts with PRO95, TYR181, and TYR188, while the pyridine ring engages in hydrophobic contacts with LEU100 and TYR318, collectively contributing to pocket complementarity and complex stability. Moreover, aromatic stacking interactions between the dimethylphenoxy aromatic ring and TYR181 further stabilize the binding conformation, while the methyl substituents reinforce hydrophobic packing within the pocket.

Figure 7

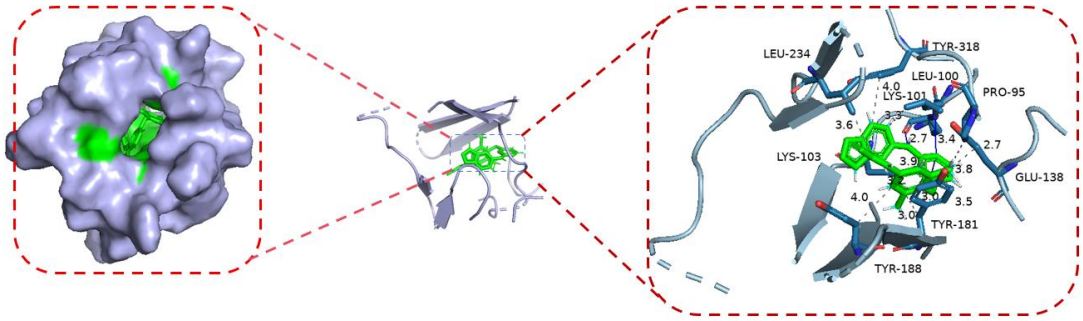

Figure_7. The docking results of compound 11 into the binding site of receptor protein.

Figure 8 shows the docking simulation results of the newly designed molecule A03. Analysis reveals that A03 forms hydrogen bond interactions with the amino acid residues LYS103 and HIS235 of the target protein, with bond lengths of 2.16 Å and 2.08 Å, respectively. This interaction contributes to enhancing the binding affinity and binding strength between the drug molecule and the target, serving as a crucial foundation for exerting pharmacological effects. Furthermore, A03 also engages in hydrophobic interactions with residues such as VAL179, TYR181, TYR188, and PHE227. Multiple hydrophobic groups synergistically bind to the pocket, which restricts the conformational motion (such as rotation or flipping) of the drug molecule within the binding cavity. This enables the molecule to stably maintain its pharmacophore conformation, thereby preventing a decrease in activity caused by conformational changes. Notably, the chloride ions on the dichlorophenyl group of A03 also form halogen bonds with residues VAL106 and GLN222. This interaction further enhances binding affinity and specificity, prompting the molecule to embed more accurately into the binding pocket of the target protein and improving its drug-likeness potential.

Figure 8

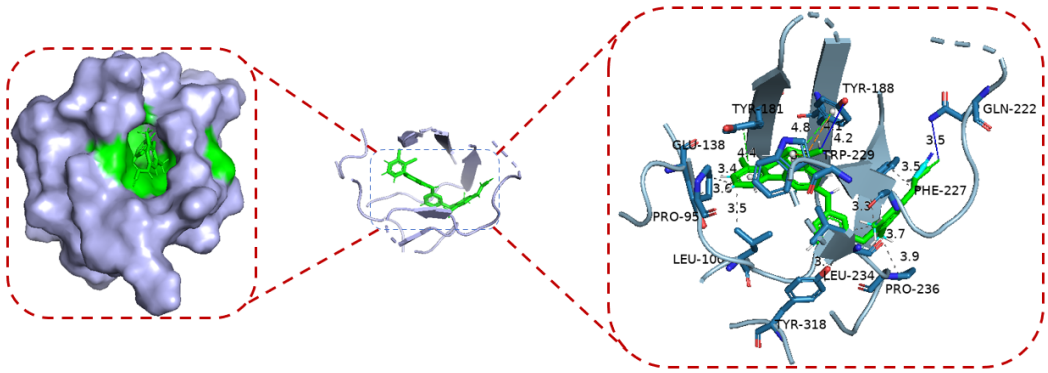

Figure_8. The docking results of compound A03 into the binding site of receptor protein.

Figure 9

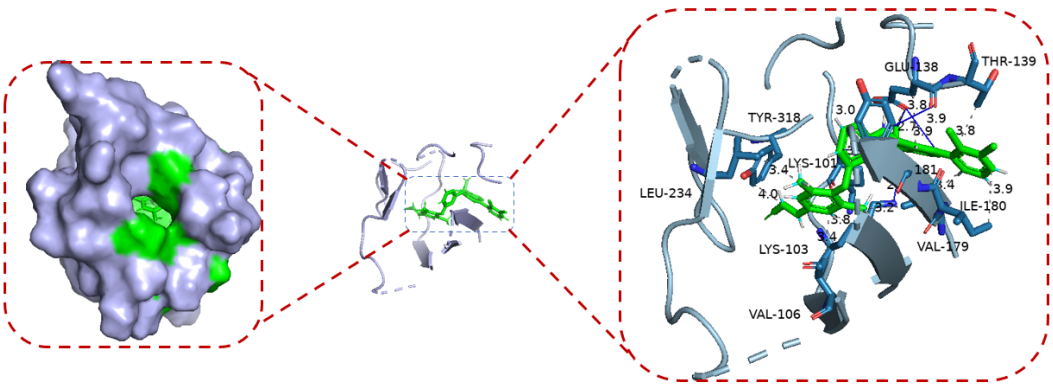

Figure_9. The docking results of compound A04 into the binding site of receptor protein.

Figure 9 presents the docking simulation results of the newly designed molecule A04. Analysis shows that A04 forms a hydrogen bond network with the amino acid residues LYS101, LYS103, and GLU138 via its sulfonamide group; additional aromatic packing (e.g., π-π) with residues around the NNRTI pocket further stabilizes the complex. Furthermore, the phenoxy group and dichlorobenzene structural moiety in A04 engage in hydrophobic interactions with multiple residues such as VAL106, THR139, VAL179, and ILE180. These synergistic hydrophobic interactions collectively enhance the stability of the complex. In addition, A04 exhibits favorable polar/electrostatic contacts with charged residues such as GLU138 and LYS101, which may further support the binding affinity and maintain the pharmacophore geometry within the pocket.

3.5 Results of MD simulation

To further investigate the interaction mechanism and binding stability between small-molecule ligands and the target protein, we performed 100 ns MD simulations on the complex systems obtained from molecular docking using GROMACS 2019.6 software. Based on the simulation results and combined with biological activity data, we selected Compound 11 (template compound), A03 (the newly designed molecule with the highest activity), and A04 (the one with the lowest activity) as representative ligands, and conducted detailed analyses on their complexes with the protein (8FE8-11, 8FE8-A03, and 8FE8-A04). Relevant results are shown in Figure 10.

RMSD is a key indicator for evaluating the degree of deviation of protein backbone atoms from the initial conformation, and is commonly used to assess the overall structural stability of a system during simulation.[46] As shown in Figure 10a, all three RMSD curves rose rapidly in the early stage of the simulation (0-20 ns), then entered a stable phase and fluctuated slightly around a certain value. Specifically, the RMSD of 8FE8-11 stabilized at 0.25±0.03 nm with a fluctuation amplitude of only 0.06 nm; 8FE8-A03 stabilized at 0.30±0.05 nm with a fluctuation amplitude of 0.10 nm; and 8FE8-A04 stabilized at 0.28±0.04 nm with a fluctuation amplitude of 0.08 nm. This indicates that all three systems have completed conformational relaxation and reached dynamic equilibrium without significant structural drift, validating the reliability of the MD simulations. Notably, complex 8FE8-11 (light green curve) exhibited a narrower fluctuation range throughout the simulation, while the RMSD fluctuations of 8FE8-A03 (dark green) and 8FE8-A04 (purple) were relatively larger. This suggests that the complex formed by the template compound 11 and the protein possesses higher overall structural stability, whereas the newly designed molecules A03 and A04 demonstrated greater conformational flexibility.

RMSF is used to evaluate the local flexibility of individual residues during the simulation, and the results are shown in Figure 10b. The results revealed that the RMSF curves of the three complexes exhibited a highly similar overall trend, with the RMSF values of all residues below 0.75 nm, and particularly slight fluctuations in the key binding regions. This phenomenon indicates that these ligands adopted relatively consistent binding modes with the protein, and the residues in the key binding regions possessed high conformational stability. No local structural disorder caused by ligand binding was observed, and similar dynamic behaviors and binding characteristics were maintained.

Overall, the MD simulation results indicate that the newly designed compounds, guided by 3D-QSAR models and combined with molecular docking predictions, can effectively bind to the 8FE8 protein and form stable complexes. Although their structural stability is slightly lower than that of the template compound, they still maintain binding behaviors and dynamic characteristics similar to the parent molecule, providing robust theoretical support for subsequent optimization.

Figure 10

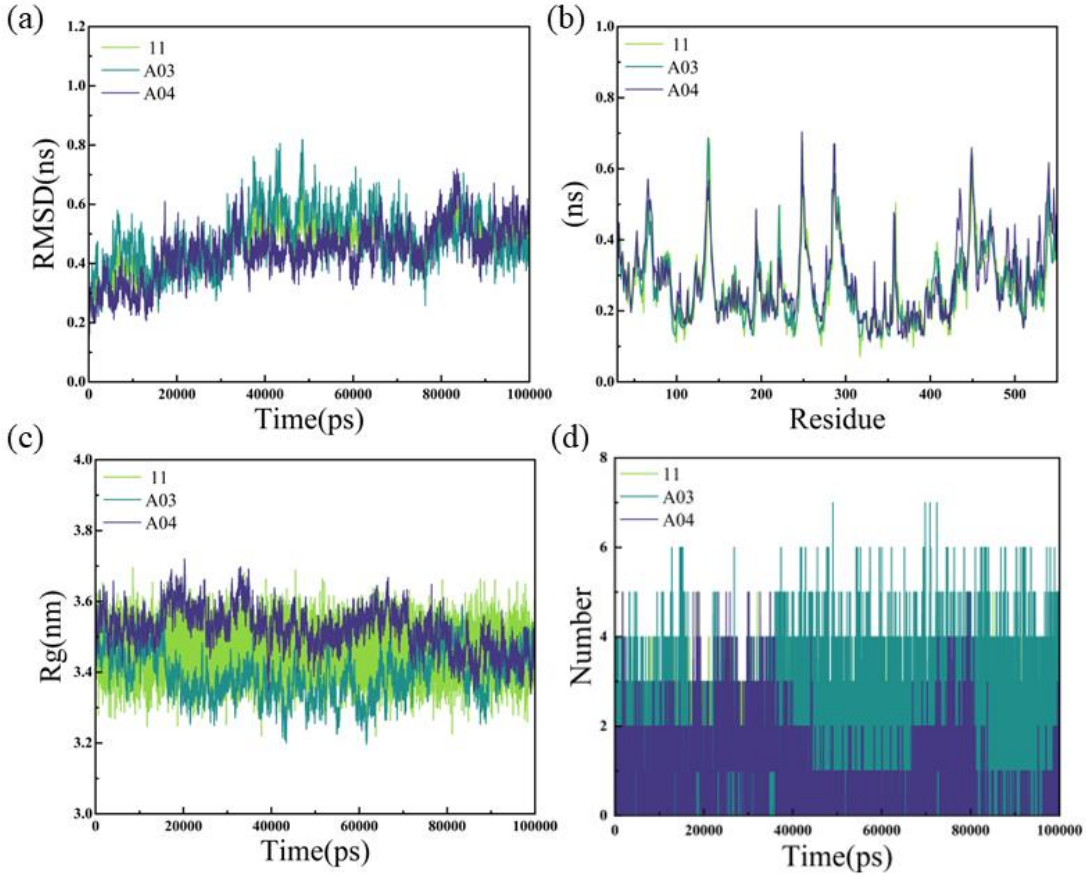

Figure_10. Results of 100 ns MD simulations for complexes 8FE8-11 (light green), 8FE8-A03 (dark green), and 8FE8-A04 (purple). (a) RMSD values of the complex proteins. (b) RMSF of residues in the three protein-ligand complexes. (c) Radius of gyration for the three protein-ligand complexes. (d) Number of hydrogen bonds formed between 8FE8 and the ligands.

3.6 Binding free energy analysis

To further investigate the binding affinity between ligands and the protein, the binding free energies of the three ligand-protein systems were calculated using the gmx_MMPBSA program, based on the 100 ns MD simulation performed. The results are presented in Table 5. Among them, Compound 11 exhibited a binding free energy of -15.07 kJ·mol^{-1}, while the newly designed Compounds A03 and A04 showed binding free energies of -26.37 kJ·mol^{-1} and -19.78 kJ·mol^{-1}, respectively. Generally, the more negative the binding free energy of a complex, the higher the binding stability between the ligand and the target protein, and the better the corresponding ligand activity.[47] The binding free energies of the three systems follow the order: 8FE8-11 > 8FE8-A04 > 8FE8-A03. This is consistent with the predictions of the 3D-QSAR models (Compound 11 < Compound A04 < Compound A03), further validating the rationality of the molecular design strategy. Furthermore, the van der Waals energy (ΔE_{VDW}) was found to be the dominant contributor to ΔG_{bind} (binding free energy) across all systems, as interactions between ligands and amino acids in the active pocket primarily occur in the form of van der Waals forces. Secondly, electrostatic energy (ΔE_{ELE}) and non-polar solvation energy (ΔG_{surf}) also play positive roles in ΔG_{bind}. Overcoming the positive value of polar solvation energy (ΔG_{GB}) is one of the key approaches to enhance the binding affinity between the compound (ligand) and the protein.

Table 5. Combined free energy and different energy contributions

Complex	ΔE_{ELE} (KJ mol^{-1})	ΔE_{VDW} (KJ mol^{-1})	ΔG_{GB} (KJ mol^{-1})	ΔG_{surf} (KJ mol^{-1})	ΔG_{bind} (KJ mol^{-1})
8FE8-11	-8.28	-26.72	24.72	-4.79	-15.07
8FE8-A03	-72.40	-27.61	58.70	-3.38	-26.37
8FE8-A04	-45.07	-20.33	77.59	-4.79	-19.78

3.7 FEL analysis

FEL is useful for describing the variation of free energy in complexes during MD simulations. By calculating the free energy profile of protein-ligand complexes, the conformational distribution and stability of the complexes can be reflected. The free energy profiles between RMSD and Rg of Compounds 11, A03, and A04 are shown in Figure 11. The color range from red to dark blue represents free energy, with a darker color indicating a more stable conformation; blue corresponds to low free energy with stable conformations, while red denotes high free energy with metastable conformations. All three graphs in Figure 11 show that the system has a low free energy core region converging in a "funnel shape", which indicates that the existence of a globally stable conformation is a common feature of the system. The FEL graph of Compound 11 presents a single and narrow straight well, which is consistent with its small RMSD fluctuation and also reflects the strong structural stability of the complex. In contrast, the FEL graphs of A03 and A04 exhibit similarity. This may be because, as newly designed molecules, they share similarities in structural modification strategies. For instance, both incorporate dichlorobenzene groups and form hydrogen bonds with LYS103, leading to convergent conformational dynamic ranges and stable conformational distribution patterns when binding to the protein. Both molecules also show stronger conformational flexibility than Compound 11.

Figure 11

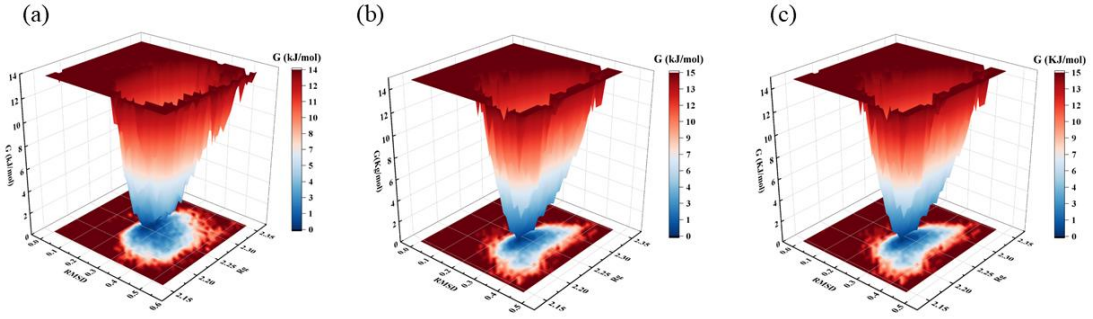

Figure_11. FEL plots of (a) 11. (b) A03. (c) A04.

3.8 ADMET predicted results

In this study, eight newly designed drug molecules were systematically evaluated using online ADMET prediction tools, with the results summarized in Table 6 and Figure 12. The predictions revealed that all eight molecules exhibited favorable intestinal absorption capacity, with absorption rates ranging from 83.86% to 94.80%. This indicates their ability to efficiently penetrate the intestinal mucosal barrier and enter the bloodstream, suggesting promising potential for oral bioavailability. In terms of metabolism, these molecules are likely to be metabolized primarily via the CYP450 enzyme system (including CYP2D6, 3A4, 1A2, 2C19, 2C9, etc.), implying diverse metabolic pathways. Regarding clearance properties, the evaluation results indicated that the compounds can be cleared via hepatic and renal pathways, with low predicted total clearance rates. This suggests they undergo slow clearance and prolonged retention *in vivo*, which is conducive to maintaining effective therapeutic concentrations. Integrating the above pharmacokinetic properties, the newly designed drug molecules demonstrated favorable characteristics in absorption, metabolism, and clearance, exhibiting favorable drug-likeness and potential for clinical translation.

Table 6. ADMET Properties of Compound 11 and Novel Design Molecules

			Metabolism CYP							Excretion	Toxicity		
			2D6	3A4	1A2	2C19	2C9	2D6	3A4	Total clearance (log mL $min^{-1}kg^{-1}$)			
NO.	Absorption	Distribution	Substrate				Inhibitor				AMES	Hepatotoxicity	Skin sensitization
11	91.882	0.351	No	Yes	No	Yes	No	No	Yes	0.422	No	Yes	No
A01	90.352	0.344	No	Yes	No	Yes	Yes	No	Yes	-0.272	No	Yes	No
A02	84.439	0.018	No	Yes	No	No	Yes	No	Yes	0.039	No	Yes	No

A03	94.806	0.587	No	Yes	No	Yes	Yes	No	Yes	-0.119	No	Yes	No
A04	83.864	0.344	No	Yes	No	No	Yes	No	Yes	-0.201	No	Yes	No
A05	86.954	0.658	No	Yes	No	Yes	Yes	No	Yes	-0.005	No	Yes	No
A06	88.163	0.250	No	Yes	No	No	Yes	No	Yes	-0.319	No	Yes	No
A07	87.053	1.418	No	Yes	No	No	No	No	Yes	0.489	No	Yes	No
A08	90.262	0.866	No	Yes	No	No	No	No	Yes	0.038	No	Yes	No

Figure 12

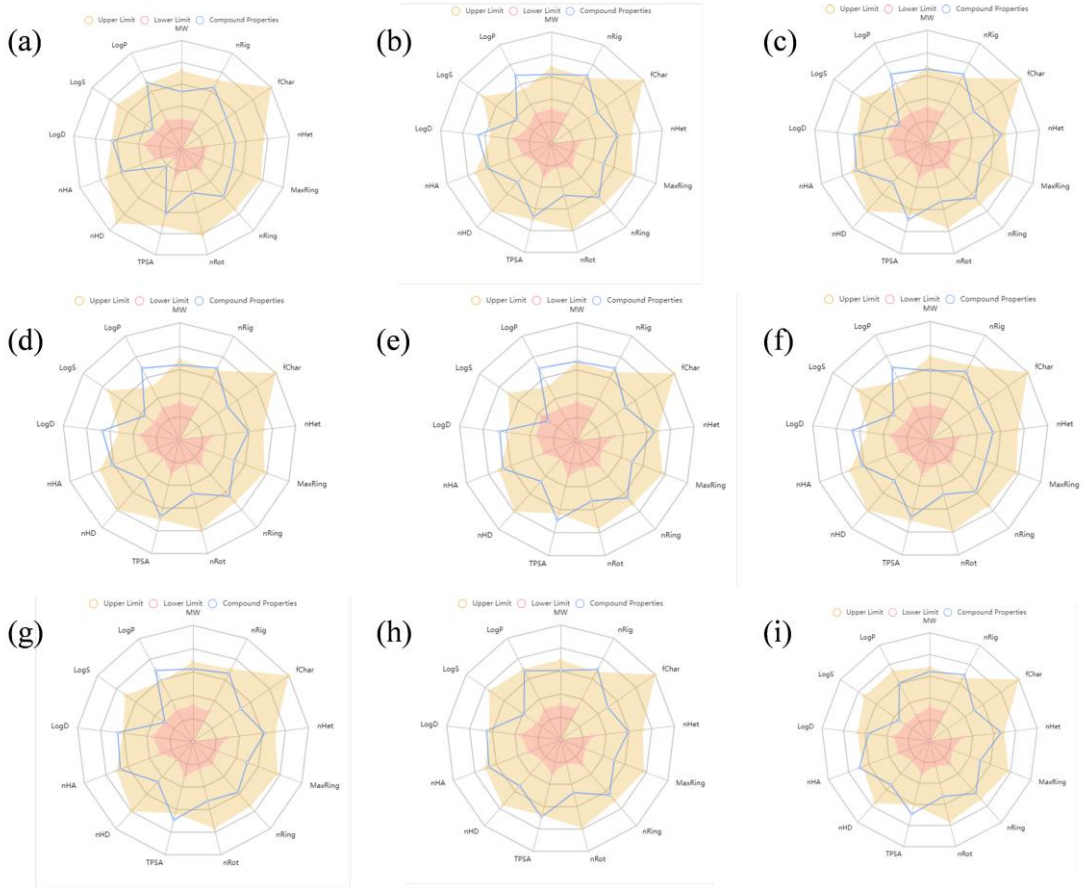

Figure_12. Physical properties of the newly designed compounds. (a) Physical properties of compound 11. (b) Physical properties of A01. (c) Physical properties of A02. (d) Physical properties of A03. (e) Physical properties of A04. (f) Physical properties of A05. (g) Properties of A06. (h) Physical properties of A07. (i) Physical properties of A08.

IV. Conclusions

In this work, DAPY derivatives were investigated as potential HIV-1 RT inhibitors through an integrated in silico workflow combining 3D-QSAR modeling, molecular docking, MD simulations, and ADMET prediction. Reliable 3D-QSAR models were established and validated, where the CoMFA model characterized steric and electrostatic contributions, and the CoMSIA model further considered electrostatic, hydrophobic, and hydrogen-bond donor features. The corresponding 3D contour maps delineated activity-favorable and activity-unfavorable regions, thereby providing interpretable guidance for substituent optimization. Guided by these SAR insights, eight new DAPY derivatives were designed using the most active compound 11 (pEC_{50} = 8.721) as the template, and all designed molecules showed higher predicted activity than the template. Structure-based analyses further supported the design rationale. Docking results indicated that the DAPY derivatives adopt stable binding

conformations within the RT pocket and form tight interactions with key residues, consistent with enhanced complex stability. To evaluate dynamic stability, 100 ns MD simulations were performed, showing rapid equilibration of the ligand-protein systems; the protein backbone remained stable with moderate flexibility, and the ligands exhibited only minor conformational adjustments while remaining bound in the pocket. MM/PBSA binding free energy estimates were in good agreement with the 3D-QSAR predictions, providing additional support for the predictive reliability of the models. Finally, ADMET evaluation suggested favorable drug-like potential for the designed molecules, with predicted intestinal absorption ranging from 83.86% to 94.80% and no hepatotoxicity or skin sensitization alerts, while experimental validation *in vitro* and *in vivo* remains necessary. Collectively, these results provide computationally guided candidates and SAR insights for further optimization of DAPY-based HIV-1 RT inhibitors.

Author Contributions

Xi He: Writing - original draft, Writing - review & editing, Simulation, **Yankai Li**: Investigation, **Ping Cheng**: Data curation and Resources. **Pingshu Zhang**: Project administration, and Resources.

Conflicts of interest

There are no conflicts of interest to declare.

Data Availability Statements

The data that support the findings of this study are available from the corresponding author upon reasonable request.

Funding

This research received no external funding

References

[1] J. Dai, X. Jiang, H. Gao, et al., Discovery of novel fused-heterocycle-bearing diarypyrimidine derivatives as HIV-1 potent NNRTIs targeting tolerant region I for enhanced antiviral activity and resistance profile, Eur J Med Chem. 281(2025)117033. https://doi.org/10.1016/j.ejmech.2024.117033.

[2] R. D. Govender, M. J. Hashim, M. A. Khan, et al., Global Epidemiology of HIV/AIDS: A Resurgence in North America and Europe, J Epidemiol Glob Health. 11(2021)296. https://doi.org/10.2991/jegh.k.210621.001.

[3] L. Menendez-Arias and R. Delgado, Update and latest advances in antiretroviral therapy, Trends Pharmacol Sci. 43(2022)16. https://doi.org/10.1016/j.tips.2021.10.004.

[4] Y. Zhang, L. Chen, Z. Wang, et al., Design of novel DABO derivatives as HIV-1 RT inhibitors using molecular docking, molecular dynamics simulations and ADMET properties, J Biomol Struct Dyn. 42(2024)4196-4213. https://doi.org/10.1080/07391102.2023.2219331.

[5] P. Braun, R. Delgado, M. Drago, et al., A European multicientre study on the comparison of HIV-1 viral loads between VERIS HIV-1 Assay and Roche COBAS(R) TAQMAN(R) HIV-1 test, Abbott RealTime HIV-1 Assay, and Siemens VERSANT HIV-1 Assay, J Clin Virol. 92(2017)75. http://dx.doi.org/10.1016/j.jcv.2017.05.003.

[6] A. O. Pasternak, M. L. Grijsen, F. W. Wit, et al., Cell-associated HIV-1 RNA predicts viral rebound and disease progression after discontinuation of temporary early ART, JCI Insight. 5(2020)e134196. https://doi.org/10.1172/jci.insight.134196.

[7] A. O. Pasternak, M. de Bruin, S. Jurriaans, et al., Modest nonadherence to antiretroviral therapy promotes residual HIV-1 replication in the absence of virological rebound in plasma, J Infect Dis. 206(2012)1443. https://doi.org/10.1093/infdis/jis502.

[8] A. O. Pasternak, S. Jurriaans, M. Bakker, et al., Cellular levels of HIV unspliced RNA from patients on combination antiretroviral therapy with undetectable plasma viremia predict the therapy outcome, PLoS One. 4(2009)e8490. https://doi.org/10.1371/journal.pone.0008490.

[9] E. Chiappini, E. Berti, K. Gianesin, et al., Pediatric human immunodeficiency virus infection and cancer in the highly active antiretroviral treatment (HAART) era, Cancer Lett. 347(2014)38. https://doi.org/10.1016/j.canlet.2014.02.002.

[10] D. Kang, D. Feng, T. Ginex, et al., Exploring the hydrophobic channel of NNIBP leads to the discovery of novel piperidine-substituted thiophene[3,2-d]pyrimidine derivatives as potent HIV-1 NNRTIs, Acta Pharmaceutica Sinica B. 10(2020)878. https://doi.org/10.1016/j.apsb.2019.08.013.

[11] Y. Yang, D. Kang, L. A. Nguyen, et al., Structural basis for potent and broad inhibition of HIV-1 RT by thiophene[3,2-d]pyrimidine non-nucleoside inhibitors, Elife. 7(2018)e36340. https://doi.org/10.7554/eLife.36340.001.

[12] A. Carr, N. E. Mackie, R. Paredes, et al., HIV drug resistance in the era of contemporary antiretroviral therapy: A clinical perspective, Antivir Ther. 28(2023)1. https://doi.org/10.1177/13596535231201162.

[13] M. E. Cilento, K. A. Kirby and S. G. Sarafianos, Avoiding Drug Resistance in HIV Reverse Transcriptase, Chemical Reviews. 121(2021)3271-3296. https://doi.org/10.1021/acs.chemrev.0c00967.

[14] P. Gao, S. Song, Z. Wang, et al., Design, synthesis and anti-HIV evaluation of novel 5-substituted diarylpyrimidine derivatives as potent HIV-1 NNRTIs, Bioorg Med Chem. 40(2021)116195. https://doi.org/10.1016/j.bmc.2021.116195.

[15] S. Yang, C. Pannecouque, D. Daelemans, et al., Molecular design, synthesis and biological evaluation of BP-O-DAPY and O-DAPY derivatives as non-nucleoside HIV-1 reverse transcriptase inhibitors, Eur J Med Chem. 65(2013)134. http://dx.doi.org/10.1016/j.ejmech.2013.04.052.

[16] Y. Sang, C. Pannecouque, E. De Clercq, et al., Chemical space exploration of novel naphthyl-carboxamide-diarylpyrimidine derivatives with potent anti-HIV-1 activity, Bioorg Chem. 111(2021)104905. https://doi.org/10.1016/j.bioorg.2021.104905.

[17] S. Han, Y. Sang, Y. Wu, et al., Fragment hopping-based discovery of novel sulfinylacetamide-diarylpyrimidines (DAPYs) as HIV-1 nonnucleoside reverse transcriptase inhibitors, Eur J Med Chem. 185(2020)111874. https://doi.org/10.1016/j.ejmech.2019.111874.

[18] X. Jin, L.-M. Zhao, S. Wang, et al., Structure-Based Discovery of Novel NH2-Biphenyl-Diarylpyrimidines as Potent Non-Nucleoside Reverse Transcriptase Inhibitors with Significantly Improved Safety: From NH2-Naphthyl-Diarylpyrimidine to NH2-Biphenyl-Diarylpyrimidine, Journal of Medicinal Chemistry. 65(2022)8478. https://doi.org/10.1021/acs.jmedchem.2c00468.

[19] D. Feng, X. Zuo, F. Zhao, et al., Identification of "dual-site"-binding diarylpyrimidines targeting both NNIBP and the NNRTI adjacent site of the HIV-1 reverse transcriptase, Eur J Med Chem. 247(2023)115045. https://doi.org/10.1016/j.ejmech.2022.115045.

[20] H. Jiang, Y. Li, Z. Wang, et al., 3D-QSAR, molecular docking, and molecular dynamics analysis of novel biphenyl-substituted pyridone derivatives as potent HIV-1 NNRTIs, Journal of Biomolecular Structure and Dynamics. 42(2023)13603.

https://doi.org/10.1080/07391102.2023.2276885.
[21] X. Zhao, R. Zhang, X. Yu, et al., Discovery of novel tubulin polymerization inhibitors by utilizing 3D-QSAR, molecular docking and molecular dynamics simulation, New Journal of Chemistry. 46(2022)16426. https://doi.org/10.1039/d2nj02773a.
[22] Y. Wang, Y. Guo, S. Qiang, et al., 3D-QSAR, Molecular Docking, and MD Simulations of Anthraquinone Derivatives as PGAM1 Inhibitors, Front Pharmacol. 12(2021)764351. https://doi.org/10.3389/fphar.2021.764351.
[23] F. Xiong, L. Chen, Y.-j. Zhang, et al., Molecular Modeling and Docking Studies of 2,4,5-Trisubstituted Pyrimidines as HIV-1 Non-Nucleoside Reverse Transcriptase Inhibitors, Polycyclic Aromatic Compounds. 43(2023)7870. https://doi.org/10.1080/10406638.2022.2141274.
[24] L. Chen, Y. Zhang, Z. Wang, et al., Drug Design, Molecular Docking and Molecular Dynamics Simulations of Indole Class HIV-1 NNRTIs Explored with QSAR and Topomer Search, ChemistrySelect. 8(2023)e202300759. https://doi.org/10.1002/slct.202300759.
[25] Z. Lian, H. Si, H. Xia, et al., Tit Structure-activity Relationship Study and Design of Novel 1, 8- Naphthimide Derivatives as Potential DNA-targeting Chemotherapeutic Agents for Osteosarcoma, Med Chem. 19(2023)906. https://doi.org/10.2174/1573406419666230414144825.
[26] S. Durdagi, T. Mavromoustakos, N. Chronakis, et al., Computational design of novel fullerene analogues as potential HIV-1 PR inhibitors: Analysis of the binding interactions between fullerene inhibitors and HIV-1 PR residues using 3D QSAR, molecular docking and molecular dynamics simulations, Bioorg Med Chem. 16(2008)9957. https://doi.org/10.1016/j.bmc.2008.10.039.
[27] W. Sippl and H. D. Höltje, Structure-based 3D-QSAR—merging the accuracy of structure-based alignments with the computational efficiency of ligand-based methods, Journal of Molecular Structure: THEOCHEM. 503(2000)31. https://doi.org/10.1016/S0166-1280(99)00361-9.
[28] M. Sadeghzadeh, M. Salahinejad, N. Zarezadeh, et al., Antitumor evaluation and 3D-QSAR studies of a new series of the spiropyrroloquinoline isoindolinone/aza-isoindolinone derivatives by comparative molecular field analysis (CoMFA), Mol Divers. 21(2017)821. https://doi.org/10.1007/s11030-017-9778-z.
[29] H. R. Xu, L. Fu, P. Zhan, et al., 3D-QSAR analysis of a series of S-DABO derivatives as anti-HIV agents by CoMFA and CoMSIA, SAR and QSAR in Environmental Research. 27(2016)999. https://doi.org/10.1080/1062936X.2016.1233580.
[30] U. A. Gerhard Klebe, Comparative Molecular Similarity Index Analysis (CoMSIA) to study hydrogen-bonding properties and to score combinatorial libraries, Journal of Computer-Aided Molecular Design. 13(1999)1.
[31] K. Roy, On some aspects of validation of predictive quantitative structure–activity relationship models, Expert Opinion on Drug Discovery. 2(2007)1567. https://doi.org/10.1517/17460441.2.12.1567.
[32] F. Xiong, Y. J. Zhang, H. Y. Jiang, et al., Exploring the Efficacy of Noncovalent SARS-CoV-2 Main Protease Inhibitors: A Computational Simulation Analysis Study, Chem Biodivers. 21(2024)e202302089. https://doi.org/10.1002/cbdv.202302089.
[33] P. P. Qian, S. Wang, K. R. Feng, et al., Molecular modeling studies of 1,2,4-triazine derivatives as novel h-DAAO inhibitors by 3D-QSAR, docking and dynamics simulations, RSC Advances. 8(2018)14311. https://doi.org/10.1039/c8ra00094h.
[34] H. Jiang, J. Xu, Z. Wang, et al., Design of novel anti-MRSA inhibitors: a computational study integrating QSAR, ADMET, and molecular dynamics simulations, New Journal of Chemistry. 48(2024)16877. https://doi.org/10.1039/d4nj03247k.
[35] Y. Tuo, G. Li, Z. Liu, et al., Discovery of novel antifungal resorcylate aminopyrazole Hsp90 inhibitors based on structural optimization by molecular simulations, New Journal of Chemistry. 46(2022)4890. https://doi.org/10.1039/d1nj04927e.
[36] X. Y. Meng, H. X. Zhang, M. Mezei, et al., Molecular docking: a powerful approach for structure-based drug discovery, Curr Comput Aided Drug Des. 7(2011)146. https://doi.org/10.2174/157340911795677602.
[37] M. A. Lill and M. L. Danielson, Computer-aided drug design platform using PyMOL, J Comput Aided Mol Des. 25(2011)13. https://doi.org/10.1007/s10822-010-9395-8.
[38] S. Yuan, H. C. S. Chan and Z. Hu, Using PyMOL as a platform for computational drug design, WIREs Computational Molecular Science. 7(2017)e1298. https://doi.org/10.1002/wcms.1298.
[39] T. U. da Silva, K. d. C. Pougy, M. G. Albuquerque, et al., Development of parameters compatible with the CHARMM36 force field for [Fe4S4]2+ clusters and molecular dynamics simulations of adenosine-5'-phosphosulfate reductase in GROMACS 2019, Journal of Biomolecular Structure and Dynamics. 40(2022)3481. https://doi.org/10.1080/07391102.2020.1847687.
[40] L. Chen, W.-G. Liu, F. Xiong, et al., 3D-QSAR, molecular docking and molecular dynamics simulations analyses of a series of heteroaryldihydropyrimidine derivatives as hepatitis B virus capsid assembly inhibitors, New Journal of Chemistry. 45(2021)22062. https://doi.org/10.1039/d1nj02542b.
[41] E. Wang, H. Sun, J. Wang, et al., End-Point Binding Free Energy Calculation with MM/PBSA and MM/GBSA: Strategies and Applications in Drug Design, Chem Rev. 119(2019)9478. https://doi.org/10.1021/acs.chemrev.9b00055.
[42] M. Segall, Advances in multiparameter optimization methods for de novo drug design, Expert Opinion on Drug Discovery. 9(2014)803. https://doi.org/10.1517/17460441.2014.913565.
[43] G. Xiong, Z. Wu, J. Yi, et al., ADMETlab 2.0: an integrated online platform for accurate and comprehensive predictions of ADMET properties, Nucleic Acids Res. 49(2021)5. https://doi.org/10.1093/nar/gkab255.
[44] D. E. V. Pires, T. L. Blundell and D. B. Ascher, pkCSM: Predicting Small-Molecule Pharmacokinetic and Toxicity Properties Using Graph-Based Signatures, Journal of Medicinal Chemistry. 58(2015)4066. https://doi.org/10.1021/acs.jmedchem.5b00104.
[45] J. P. James, K. Ishwar Bhat, U. A. More, et al., Design, synthesis, molecular modeling, and ADMET studies of some pyrazoline derivatives as shikimate kinase inhibitors, Medicinal Chemistry Research. 27(2017)546. https://doi.org/10.1007/s00044-017-2081-9.
[46] K. Sargsyan, C. Grauffel and C. Lim, How Molecular Size Impacts RMSD Applications in Molecular Dynamics Simulations, J Chem Theory Comput. 13(2017)1518. https://doi.org/10.1021/acs.jctc.7b00028.
[47] B. R. Miller, T. D. McGee, J. M. Swails, et al., MMPBSA.py: An Efficient Program for End-State Free Energy Calculations, Journal of Chemical Theory and Computation. 8(2012)3314. https://doi.org/10.1021/ct300418h.